Geochimica et Cosmochimica Acta, Vol. 69, No. 11, pp. 2797–2812, 2005

0016-7037/05 $30.00 + .00

doi:10.1016/j.gca.2004.12.008

Influence of pH on the interlayer cationic composition and hydration state of Ca-montmorillonite: Analytical chemistry, chemical modelling and XRD profile modelling study

Eric Ferrage,[1,2,*] Christophe Tournassat,[2,3] Emmanuel Rinnert,[2,4] and Bruno Lanson[1]

[1]Environmental Geochemistry Group, LGIT, University of Grenoble-I P.O. Box 53, 38041 Grenoble, France
[2]ANDRA, Parc de la Croix Blanche, 1/7 rue Jean Monnet, 92298 Châtenay-Malabry Cedex, France
[3]BRGM, 3 avenue Claude Guillemin, 45060 Orléans Cedex 2, France
[4]Laboratoire de Chimie Physique et Microbiologie pour l'Environnement, UMR 7564 CNRS-Université Henri Poincaré, 405 rue de Vandoeuvre, 54600 Villers-Lès-Nancy, France

(*Received July* 23, 2004; *accepted in revised form December* 6, 2004)

Abstract—The hydration state of a <2 μm fraction of Ca-saturated SWy-2 montmorillonite was characterised after rapid equilibration (3 hours) under pH-controlled conditions (0.1–12.6 pH range). The solution composition was monitored together with the interlayer composition and X-ray diffraction (XRD) patterns were recorded on oriented preparations. Experimental XRD patterns were then fitted using a trial-and-error procedure to quantify the relative proportions of layers with different hydration states.

The montmorillonite is mostly bi-hydrated in basic and near-neutral conditions whereas it is mostly mono-hydrated at low pH. The transition from the bi-hydrated to the mono-hydrated state occurs through very heterogeneous structures. However, the proportion of the different layer types determined from XRD profile modelling and that derived from chemical modelling using Phreeqc2 code strictly coincide. This correlation shows that the hydration modification is induced by a H_3O^+-for-Ca^{2+} exchange at low pH, the two species being distributed in different interlayers. This layer-by-layer exchange process occurs randomly in the layer stack.

Under alkaline conditions, results from XRD profile modelling and from near infrared diffuse reflectance spectroscopy (NIR-DRS) clearly demonstrate that there is no $CaOH^+$-for-Ca^{2+} exchange at high pH. The apparent increase in Ca sorption in smectite interlayers with increasing pH is thus probably related to the precipitation of Calcium-Silicate-Hydrate (CSH) phases, which also accounts for the decrease in Si concentration under high-pH conditions. This precipitation is thermodynamically favoured. *Copyright © 2005 Elsevier Ltd*

1. INTRODUCTION

One of the possible multi-barrier storage concepts developed in France for intermediate-level long-lived radioactive wastes (ILLW wastes) consists of vitrified waste placed in containers and overpacks, encased in exogenous materials (near-field engineered barrier) and ultimately buried in a clay-rich geological formation (far-field barrier). Bentonite, a clay material mostly constituted of smectite, is considered a promising material as an engineered barrier in the context of nuclear waste disposal. The potential of smectite stems from its mechanical self-healing ability, its low hydraulic conductivity and its high sorption capacities, the combination of which is assumed to help prevent or delay radionuclide migration. However, the initial properties of smectite could be altered significantly by storage-induced perturbations. For example, the use of concrete for waste overpacks or the oxidation of pyrite, which is often present as an accessory mineral in the relevant geological environments, can lead to a wide pH range for solutions saturating the clay-barriers.

Substitutions in either tetrahedral or octahedral sheets of the smectite structure induce a permanent negative layer charge that is balanced by the presence of hydrated cations in the interlayer space. The interlayer cation composition of smectite has been studied for many decades as a function of the composition of the solution in contact with clay surfaces (Vanselow, 1932a; Sposito, 1981 and references therein), and the thermodynamics of cation exchange have been developed specifically to model these interlayer cation compositions (Vanselow, 1932a; Sposito, 1977, 1981, 1984; Elprince et al., 1980; Shainberg et al., 1980; Shu-Yuan and Sposito, 1981; Sposito et al., 1981, 1983a, 1983b, 1999; Fletcher and Sposito, 1989; Delville, 1991; Appelo and Postma, 2000). Smectite cation exchange affinities have been established for a wide range of cations including protons, which possibly replace interlayer cations under acidic conditions (Fletcher and Sposito, 1989 and references therein).

For the most common interlayer cations, hydration of homoionic smectites has been extensively studied and it has been shown, most often from the variation of 00*l* basal reflection d-spacings, that smectite incorporates H_2O molecules in its interlayers. As a consequence, with increasing relative humidity the smectite structure "swells" in different steps corresponding to the intercalation of 0, 1, 2 or 3 layers of H_2O molecules (Nagelschmidt, 1936; Bradley et al., 1937; Mooney et al., 1952; Norrish, 1954; Walker, 1956). From these early studies, it is now accepted that the hydration ability of 2:1 phyllosilicates is controlled by factors such as the nature of the interlayer cation and the amount of layer charge and its location (octahedral vs. tetrahedral). These observations have led to different models in which crystalline swelling is controlled by the balance between the repulsive forces between adjacent 2:1 layers and the attractive forces between hydrated interlayer cations and the negatively charged sur-

* Author to whom correspondence should be addressed (eric.ferrage@obs.ujf-grenoble.fr).

face of 2:1 layers (Norrish, 1954; Van Olphen, 1965; Kittrick, 1969a, 1969b; Laird, 1996, 1999). The few studies devoted to the hydration of bi-ionic smectites [Glaeser and Méring, (1954); Levy and Francis, (1975), and Iwasaki and Watanabe, (1988) on (Na, Ca)-smectites and Mamy and Gaultier, (1979) on (K, Ca)-smectites] have shown that interlayer cations tend to distribute in distinct interlayers leading to a "demixed" state.

The present work aims at characterising the hydration state of an initially Ca-saturated montmorillonite as a function of pH to better predict smectite reactivity under disturbed chemical conditions, such as those likely to occur in the vicinity of a nuclear waste disposal. For this purpose, the combination of chemical modelling and XRD profile modelling were used to follow the exchange of Ca^{2+} cations by protons under acidic conditions. Specific X-ray diffraction modelling techniques based on a trial-and-error approach were used to refine the early descriptions of smectite hydration by taking into account the possible coexistence in the smectite structure of different layer types, each exhibiting a specific hydration state (Bérend et al., 1995; Cases et al., 1997; Cuadros, 1997; Ferrage et al., 2005a). In particular, the likely mutual exclusion of calcium and protons in smectite interlayers and the expected hydration contrast between such calcium- and proton-saturated smectite layers was used to follow the H_3O^+-for-Ca^{2+} exchange supposed to occur at low pH. The same techniques were also used to assess the possible presence of cation-hydroxide ions pairs under alkaline conditions proposed by Tournassat et al. (2004a, 2004b) and Charlet and Tournassat (2005) on the basis of cation exchange experiments and chemical modelling.

2. MATERIALS AND METHODS

2.1. Clay Material Preparation

The smectite used for this study was the SWy-2 montmorillonite reference from the Source Clays Repository of The Clay Minerals Society (http://www.agry.purdue.edu/cjohnston/sourceclays/index.html) with structural formula (Stucki et al., 1984): $[(Al_{3.01}\ Fe_{0.43}\ Mg_{0.56})(Si_{7.97}\ Al_{0.03})O_{20}(OH)_4]\ M^+_{0.72}$. Naturally, this montmorillonite is mostly Na-saturated, and exhibits a low octahedral charge deficit and extremely limited tetrahedral substitutions (Mermut and Lagaly, 2001).

Size fractionation was performed by centrifugation to obtain a suspension of the $<2\ \mu m$ size fraction. An ion-exchange process was then carried out on this clay separate at room temperature with 1 $mol.L^{-1}$ aqueous saline solution of $CaCl_2$. The SWy-2 suspension was shaken mechanically in this saline solution for 24h before separation of the solid fraction by centrifugation and addition of fresh saline solution. This step was repeated three times to ensure complete cation exchange. Excess salts were then washed by four 24h cycles, including sedimentation, removal of the supernatant and re-suspension in deionised water (milli-Q/18.2 $M\Omega\ cm^{-1}$). The clay content of the final Ca-SWy-2 suspension was found to be ~37g of clay per kg of suspension using the weighing method given by Sposito et al. (1981) and revised by Tournassat et al. (2004a).

2.2. Sample Preparation

Centrifugation tubes were precisely weighed (m_{tube} in g) with a Mettler Toledo AG285 balance. A ~3 mL aliquot of the Ca-SWy-2 suspension was introduced into each 50 mL centrifuge tube with a calibrated micropipette (V_{susp}, clay content ρ). Variable volumes of $Ca(OH)_2$ or HCl were then added to reach the desired pH after addition of deionised water to obtain a 40 mL total volume (V_{tot}). The tubes were shaken for three hours. A 15 mL suspension aliquot was then collected from each tube, precisely weighed (V_{XRD}) and used for X-ray diffraction (XRD) data collection (see below). The remaining suspension was centrifuged to separate the solution from the clay slurry.

An aliquot of supernatant fluid from each tube was further filtered (0.20 μm) before measuring the pH with a pH-microelectrode (Mettler Toledo, InLab 423). Another aliquot was filtered for Na, Ca, Si, Al, Mg and Fe concentration measurements (C^{elt}_{sol}, where *elt* represents Ca, Si, etc.) using a Perkin-Elmer Optima 3300 DV inductively coupled plasma atomic emission spectrometer (ICP-AES). Si, Al, Mg and Fe concentrations were measured on a third supernatant aliquot obtained without prior filtration to give the mass of suspended solids in the supernatant as explained in Tournassat et al. (2004a) ($m_{correction}$). On the other hand, the centrifuge tubes containing the clay slurry were weighed precisely ($m_{centrif}$) and 30 mL (V_{Amm}) of 1 M ammonium acetate were added to each tube, each tube being precisely weighed after ammonium acetate addition (m_{Amm}) and shaken for 24h. NH_4^+ cations are meant to replace Ca^{2+} cations in the smectite interlayer (e.g., Sposito et al., 1981, 1983a, 1983b) and the subsequent measurement of Ca^{2+} concentration in the supernatant solution leads to the Calcium Cation Exchange Capacity (Ca-CEC). Since some solution remained in the clay slurry (V_{slurry}) before the addition of ammonium acetate, the volume of supernatant was equal to the volume of added ammonium acetate plus this volume of solution in the slurry ($V_{Amm+slurry}$). Furthermore, the amount of Ca^{2+} present in the remaining slurry solution ($C^{Ca}_{sol} \times V_{slurry}$) must be subtracted from the amount of Ca in the supernatant ($C^{Ca}_{Amm} \times V_{Amm+slurry}$). Hence, Ca-CEC is given by the following formula (in $eq.kg^{-1}$, i.e., in mol of charge per kg of clay):

$$Ca-CEC = 2 \times \frac{C^{Ca}_{Amm} \times V_{Amm+slurry} - C^{Ca}_{sol} \times \left(m_{centrif} - m_{tube} \left(V_{susp} \times \frac{V_{tot} - V_{XRD}}{V_{tot}} \times \rho \right) \right)}{\left(V_{susp} \times \frac{V_{tot} - V_{XRD}}{V_{tot}} \times \rho \right) - m_{correction}}, \quad (1)$$

$$V_{Amm+slurry} = \frac{m_{Amm} - m_{tube} - \left(V_{susp} \times \frac{V_{tot} - V_{XRD}}{V_{tot}} \times \rho \right)}{d_{Amm}} \quad (2)$$

where volumes (V) are in L, concentrations (C) in $mol.L^{-1}$, clay content (ρ) in $g.L^{-1}$ and masses (m) in g. The density of all solutions was assumed to be equal to 1.0, except for the density of the 1 M ammonium acetate solution ($d_{Amm} = 1.077$).

2.3. Chemical Composition Modelling

The chemical modelling used in this study was performed using the Phreeqc2 code (Parkhurst and Appelo, 1999), since this versatile computer code is amenable to the various conventions used to describe cation exchange and surface complexation. The model used for cation exchange was similar to that developed by Tournassat et al. (2004a) and only the main concepts and parameters are described to simplify understanding. Cation exchange capacity of montmorillonite originates both from the presence of a permanent negative charge (σ_0) in the clay lattice resulting from octahedral and tetrahedral substitutions and from the presence of broken bonds at the edges of clay platelets, which induces a pH-dependent charge (σ_H). By combining a cation-exchange model based on the Vanselow convention (Vanselow, 1932a; Sposito, 1981) with the pH-dependent charge model developed by Tournassat et al. (2004b) for clay minerals, the evolution of the Ca-CEC value can be modelled as a function of pH. Key parameters are cation exchange selectivity coefficients (K_{int}—Table 1), clay permanent charge (σ_0), structural formula and edge surface area. The latter parameter was considered to be equal to that determined for the fine fraction of the commercial Wyoming bentonite MX80 montmorillonite ($8.5\ m^2.g^{-1}$, Tournassat et al., 2003). From the adjustment to Ca-CEC data, the σ_0 value was taken to be 0.94 mol of charge (mol_c) per kg of clay. This value is similar, within error, to the 1.0 $mol_c.kg^{-1}$ value calculated from the structural formula. In the model used, a decrease of Ca-CEC was interpreted either as a decrease of σ_H (typically from pH 4 to 10 in the present study) or as resulting from H^+ sorption in the interlayer.

Table 1. Cation exchange reaction selectivity coefficients (K_{int}) used for chemical composition modelling.

Exchange reactions	log K_{int}
$2\ HX + Ca^{2+} \Leftrightarrow CaX_2 + 2\ H^+$	0.4§
$HX + CaCl^+ \Leftrightarrow CaClX + H^+$	2.5§

§ from Tournassat et al. (2004a).

2.4. X-ray Diffraction Analysis and Profile Modelling

For XRD analysis, suspension aliquots were poured through a Millipore filter (0.4 μm) and the clay cake was then laid down on a previously weighed glass slide. The resulting oriented preparations were then dried at room temperature and the mass of smectite on the glass slide was precisely determined. XRD patterns were then recorded using a Bruker D5000 diffractometer equipped with an Ansyco rh-plus 2250 humidity control device coupled to an Anton Paar TTK450 chamber. Data collection was performed at 40% relative humidity (RH) after an homogenisation period of 15 min before the measurement. Experimental measurement parameters were 6s counting time per 0.04°2θ step. The divergence slit, the two Soller slits, the antiscatter slit and the resolution slit were 0.5°, 2.3°, 2.3°, 0.5° and 0.06°, respectively. For each sample, XRD patterns were collected over a time span not exceeding one day after glass slide preparation.

The algorithms developed initially by Sakharov and Drits (1973), Drits and Sakharov (1976) and more recently by Drits et al. (1997a) and Sakharov et al. (1999) were used to fit experimental XRD profiles over the 2–50° 2θ CuKα range using a trial-and-error approach. Instrumental and experimental factors such as horizontal and vertical beam divergences, goniometer radius, length and thickness of the oriented slides were measured and introduced without further adjustment. The mass absorption coefficient (μ*) was set to 45 $cm^2.g^{-1}$, as recommended by Moore and Reynolds (1997) for clay minerals, whereas the parameter characterising the preferred orientation of the sample (σ*) was considered as a variable parameter. The z-coordinates for all atoms within the 2:1 layer framework were set as proposed by Moore and Reynolds (1997). The z-coordinates of interlayer species for dehydrated (0W) and mono-hydrated (1W) smectite layers were also set as proposed by Moore and Reynolds (1997), in contrast to those for bi-hydrated (2W) layers, since a more realistic description of the interlayer structure is obtained by assuming a unique plane of H_2O molecules on either side of the central interlayer cation (Ferrage et al., 2005a). The distance along the c* axis from the interlayer cation plane and the H_2O molecule plane is ~1.2 Å.

Additional variable parameters include the coherent scattering domain size (CSDS) along the c*-axis, which was characterised by a maximum CSDS, set at 45 layers, and a mean CSDS value (N—Drits et al., 1997b), which was adjusted. In addition, because of the weak bonding between adjacent smectite layers, layer thickness is probably scattered about its average value. This cumulative deviation from strict periodicity, described by Guinier (1964) as a disorder of the second type and detailed later by Drits and Tchoubar (1990), can be considered as strains and was accounted for by introducing a deviation parameter (σ_z). The overall fit quality was assessed using the R_p parameter (Howard and Preston, 1989). This un-weighted parameter was preferred because it is mainly influenced by misfits on the most intense diffraction maxima such as the 001 reflection, which contains essential information on the proportions of the different layer types and on their respective layer thickness.

The fitting procedure described in detail by Ferrage et al. (2005a) was used for all experimental XRD profiles of exchanged Ca-SWy. Briefly, a main structure, periodic when possible, was used to reproduce as much as possible of the experimental XRD pattern. If necessary, additional contributions to the diffracted intensity were introduced to account for the lack of fit between calculated and experimental patterns. These extra contributions were systematically related to mixed-layered structures (MLS) containing two or three components, randomly interstratified. Up to four structures were necessary to reproduce experimental patterns, because of the very heterogeneous structures observed. However, layers with the same hydration state present in the different MLS contributing to the diffracted intensity were assumed to have identical properties to reduce the number of adjustable parameters. Specifically for a given sample, each given layer type (0W, 1W or 2W layers) was provided with a unique chemical composition, a unique layer thickness, and a unique set of atomic coordinates for all contributions. Similarly, identical values of the σ*, N and σ_z parameters were used at a given pH value for all MLSs, even though these parameters were allowed to vary as a function of pH. The relative proportions of the different MLSs and that of the different layer types in these MLSs were also considered as variable parameters during the fitting procedure.

The fitting strategy is illustrated in Figure 1 for the XRD pattern obtained for Ca-SWy-2 equilibrated in deionised water (pH = 6.41). Qualitatively, the experimental pattern exhibits well-defined diffraction maxima forming a rational series with a d_{001} value characteristic of a bi-hydrated state (~15.20 Å). However, a significant asymmetry is visible on the high-angle side of the 001 and 003 reflections and on both sides of the 005 reflection (arrows in Fig. 1a) as demonstrated by the difference plot between the experimental pattern and that calculated for the contribution of pure bi-hydrated smectite (100% of 2W layers). According to the Méring principle (Méring, 1949), the residual maximum on the high-angle side of the 001 reflection can be attributed to a MLS containing layers with a lower layer thickness in addition to 2W layers. Accordingly, a satisfactory fit (Rp = 1.45%) was obtained when a second contribution (S2–S1:S2 = 87:13), resulting from the random interstratification of 2W, 1W and 0W layers (60%, 30 and 10%, respectively—Figs. 1b, 1c), was added to the initial contribution (S1), as schematised by the pictogram shown in Figure 1d. In this pictogram, the relative proportions of the two MLSs contributing to the diffracted intensity are represented along the vertical axis by their respective surface areas whereas the proportions of the different layer types in each structure are represented on the horizontal axis. Overall, this sample contains 95% of 2W layers, 4% of 1W layers and 1% of 0W layers.

One may note that the calculated XRD patterns are not plotted over the low angle region (2θ angles lower than 5°) because the shape of the computed "background" over this angular range is not consistent with that of experimental patterns. The origin of this discrepancy is discussed by Ferrage et al. (2005a) using the recent theoretical developments made by Plançon (2002). These new insights into the real structure of clay aggregates may make it possible to reproduce experimental patterns over this angular range but they would not bring into question the results reported in the present manuscript.

2.5. Near Infrared Diffuse Reflectance Analysis

Near infrared diffuse reflectance (NIR-DR) spectra were recorded using a Perkin-Elmer 2000 FTIR spectrometer equipped with a deuterated triglycine sulphate (DTGS) detector, a tungsten-halogen source and a quartz beam-splitter. The optical device used is based on the Harrick© equipment. Diffuse reflectance spectra were recorded from 4000 to 8000 cm^{-1} with a spectral resolution of 8 cm^{-1} and obtained from the addition of 50 individual scans. Samples were placed into a Harrick© cell in which the temperature and pressure were controlled from 25 to 100 °C and from 10^{-4}–10^5 Pa, respectively. Sample temperature was measured to an accuracy greater than 0.1°C using a Pt resistance. The spectra of hydrated samples equilibrated at room humidity (40 ± 5%) were recorded first. The samples were subsequently out-gassed at 60°C for 16 hours under a residual pressure of 5.10^{-3} Pa by using a two-stage pump comprising a scroll pump and a turbomolecular pump. Two complementary gauges (Pirani and ionisation types) were used to measure the pressure from 10^{-4} Pa to room pressure. Spectra were then recorded at a sample temperature of 25°C under a residual pressure of 5.10^{-4} Pa. The diffuse reflectance, R, is defined as:

$$R = -\log \frac{I_S^D(\sigma)}{I_O^D(\sigma)} \quad (3)$$

where I_S^D is the collected diffused irradiance of the sample, I_O^D the collected diffused irradiance of the reference and σ the wavenumber. The reference was taken at 24.8°C from a potassium bromide ground powder subsequently dried under a residual pressure of 5.10^{-3} Pa.

For clay samples, the spectral domain presented in this study can be split into two regions. From 4550 to 5500 cm^{-1}, only H_2O molecules can be observed from the combinations of stretching and bending modes. From 6500 to 7500 cm^{-1}, overtones of stretching modes of all

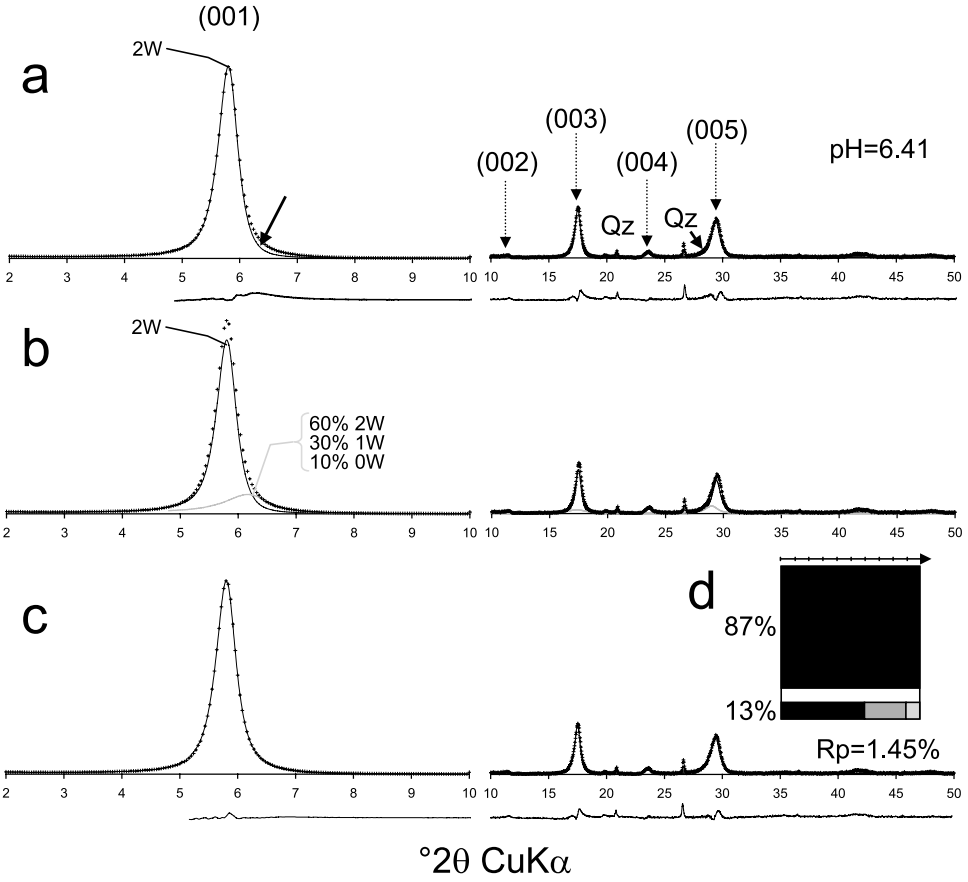

Fig. 1. Schematic description of the strategy used to fit experimental XRD patterns (see text for details). Intensities in the high-angle region (10–50°2θ) are enlarged (×10) compared to the low-angle region (4–10°2θ). Qz indicates the presence of quartz. **a)** Experimental pattern of Ca-SWy-2 sample equilibrated in deionised water (pH = 6.41) is shown as crosses whereas the XRD pattern calculated for a periodic bi-hydrated structure (100% bi-hydrated layers – 2W) is shown as a solid line. **b)** Addition of a mixed layer structure (solid grey line) with a 60:30:10 ratio between 2W:1W:0W layers. **c)** Optimum fit to the experimental pattern corresponding to the combination of the above two structures in a 87:13 ratio (solid line). **d)** Schematic representation of the structure model used to fit the experimental XRD pattern. Relative proportions, expressed in wt%, of the two elementary contributions are plotted on the *y*-axis whereas their compositions (relative proportions of the different layer types) are plotted on the *x*-axis. Light grey, dark grey and solid bars represent 0W, 1W, and 2W layers, respectively.

hydroxyl groups, both from interlayer H_2O molecules and from the silicate framework, are visible (Burneau et al., 1990; Madejova et al., 2000b). As fundamental stretching modes of hydroxyl groups have been reported previously over the 3370–3670 cm^{-1} range (Madejova et al., 2000a; Vantelon et al., 2001; Bishop et al., 2002), the frequency range calculated for the first stretching overtone extends from 6575 to 7175 cm^{-1}, assuming a 82.5 cm^{-1} anharmonicity coefficient for OH groups (Burneau and Carteret, 2000).

3. RESULTS

3.1. Cation Concentrations in Solution and in the Clay Interlayer

Concentrations of Ca, Al, Fe and Mg cations in solution are plotted as a function of pH in Figure 2. As observed in earlier studies (Baeyens and Bradbury, 1997; Tournassat et al., 2004a), the concentrations of Al, Fe and Mg in solution increase under low pH conditions as a result of clay dissolution and/or desorption processes. In addition, below a pH value of ~3, Ca concentration in solution dramatically increases as the pH decreases, although no Ca is added. At the same time, the apparent amount of Ca sorbed in the clay interlayer decreases (Fig. 3), whereas no other cation, such as Na, Al, Fe or Mg, appears to be sorbed in the interlayer from NH_4^+ exchange experiment results. With decreasing pH, Ca^{2+} is thus certainly replaced by protons in the smectite interlayer as previously hypothesized (Gilbert and Laudelout, 1965; Fletcher and Sposito, 1989; Bradbury and Baeyens, 1997; Tournassat et al., 2004b).

Under high pH conditions (pH >12), the addition of $Ca(OH)_2$ to the clay suspension leads both to an increase in the Ca concentration in solution and to an increase in the apparent Ca^{2+} sorption on smectite (Figs. 2a, 3). From these observations, and specifically from the concomitant increase in OH^- sorption, Tournassat et al. (2004a, 2004b) have hypothesized the sorption of $CaOH^+$ ion pairs in the smectite interlayers, as observed for $CaCl^+$ when ionic strength is high (Sposito et al., 1983a, 1983b; Tournassat et al., 2004b; Ferrage et al., 2005b). However, the concentration of Si in solution decreases simultaneously with the apparent increase of Ca^{2+} sorption on smectite (Fig. 3). This correlation possibly indicates the pre-

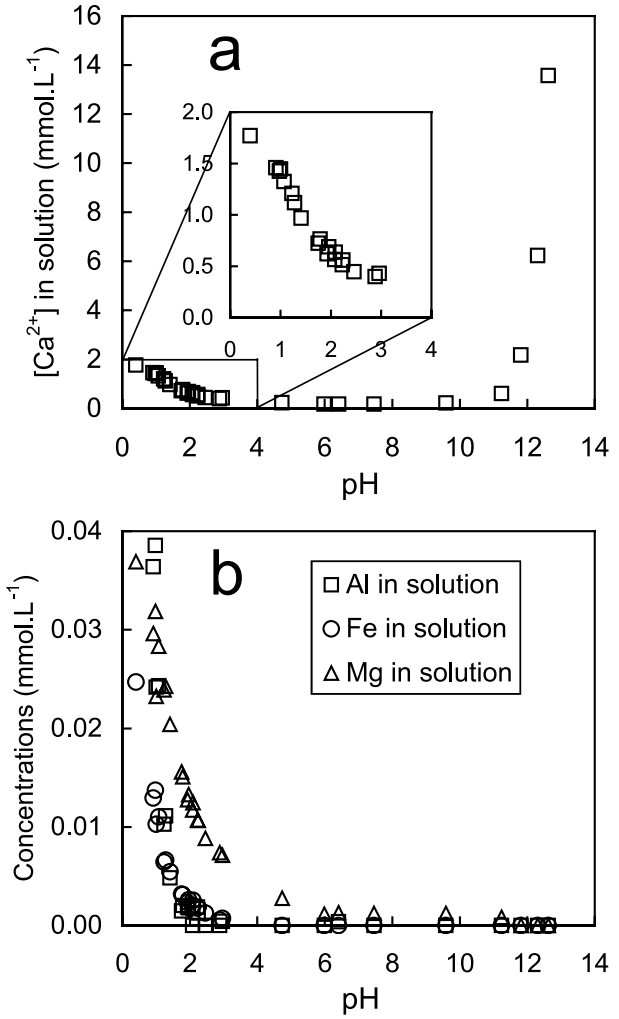

Fig. 2. Calcium concentration in solution equilibrated with clay suspension as a function of pH (**a**). Aluminium, iron and magnesium concentrations in solution equilibrated with clay suspension as a function of pH (**b**).

cipitation of a tobermorite-like Ca-Si phase at high pH (Claret et al., 2002; Tournassat et al., 2004a, 2004b) as discussed below. This hypothesis is also supported by the steady evolution of solution chemistry reported by Tournassat et al. (2004a) when working in a Na^+ ionic medium rather than in a Ca^{2+} one. However, sorption of $CaOH^+$ ion pairs cannot be differentiated from the precipitation of a Ca-Si phase on the sole basis of analytical chemistry experiments. As a consequence, modelling of XRD experiments was carried out to characterise the clay structural changes associated with the observed chemical evolutions, and to assess the various hypotheses arising from chemical modelling.

3.2. Solid Characterisation under Acidic Conditions

The qualitative observation of the 001 reflection recorded at a constant RH value (40%) for samples equilibrated at different pH values shows a dramatic modification of the smectite hydration state with decreasing pH (Fig. 4a), most probably resulting from

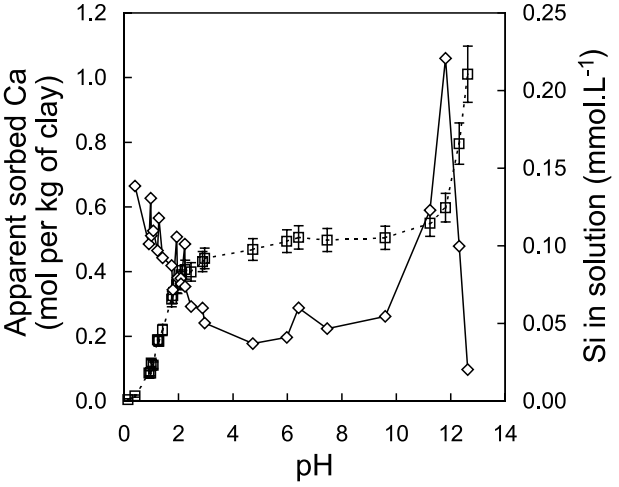

Fig. 3. Apparent amount of calcium sorbed on smectite (open squares) and Si concentration in solution (open diamonds) as a function of pH.

the modification of the smectite interlayer composition. Near neutral pH, smectite is mainly bi-hydrated (d_{001} ~ 15.2 Å), whereas at low pH values (e.g., 0.14) the presence of protons in the smectite interlayer leads to the shift of the 001 reflection towards lower d_{001} (~12.6 Å), which are characteristic of 1W smectites. When decreasing the pH from near neutral condition (pH = 6.41),

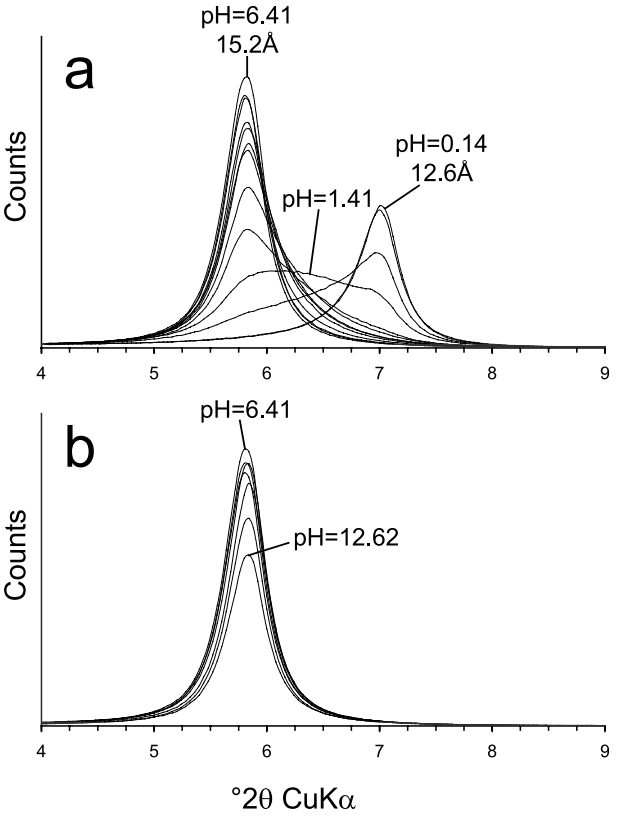

Fig. 4. Evolution of the 001 reflection of equilibrated Ca-SWy-2 as a function of pH. **a)** Under acidic conditions. **b)** Under alkaline conditions.

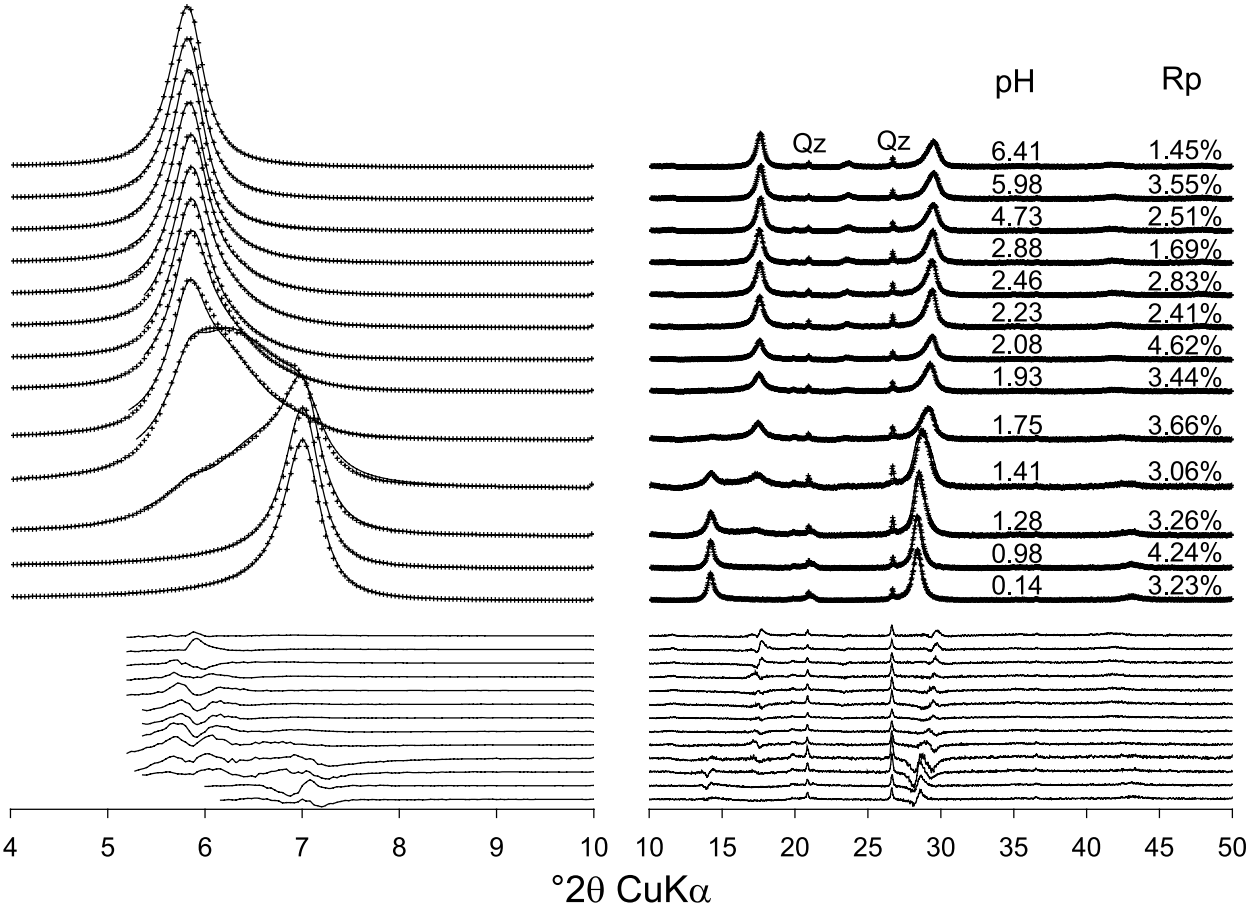

Fig. 5. Comparison between experimental and calculated XRD patterns as a function of pH under acidic conditions. Experimental XRD patterns are shown as crosses whereas the optimum fits are shown as solid lines. Qz indicates the presence of quartz.

the steady decrease of the 001 reflection intensity and the increase of the asymmetry on its high-angle side are consistent with the continuous incorporation of 1W layers. Extremely heterogeneous structures, most probably corresponding to the interstratification of 2W and 1W layers, are observed at intermediate pH values (e.g., 1.41), whereas at lower pH values, the steady increase in the 12.6 Å peak intensity and its sharpening are indicative of a homogeneous 1W state.

In the modelling of these experimental XRD patterns, it was assumed that the 1W and 2W layers correspond to smectite layers saturated with protons and Ca^{2+} cations, respectively. This hypothesis is strongly supported by the overwhelming presence of 2W layers in low-charge montmorillonite equilibrated at 40% RH (Ferrage et al., 2005a). In addition, for layers saturated by protons, it was assumed that the layer charge compensation was achieved by H_3O^+ cations, as the difference between H_3O^+ or H^+ cations could not be differentiated from the presence of an additional H_2O molecule on the midplane of the H^+-saturated interlayer. Finally, because X-ray diffraction is only sensitive to the electronic density, a simple calculation of the scattering factor for $\theta = 0$ weighted to the cation valency (η index) shows that it is not possible to differentiate, from the diffracted intensity, between interlayers saturated by Ca^{2+} or H_3O^+ cations. Ca^{2+} cations contain $18e^-$ and therefore $\eta = 9e^-$ per charge unit (c.u.) whereas for H_3O^+ ions $\eta = 10$ e^-/c.u. This calculation shows that the systematic presence of protons as interlayer cations in 1W, which was initially assumed, will not significantly impact the proportion of the different layer types derived from XRD profile modelling.

The calculated profiles are compared to the experimental patterns in Figure 5 and the relative contributions to the diffracted intensity as a function of pH are schematised in Figure 6 together with the composition of the associated MLSs. The relative contributions of the different MLSs to the diffracted intensity and their evolution as a function of pH are illustrated in Figure 7 for characteristic XRD patterns. Additional structural parameters, such as the layer thickness of the different layer types, their content of H_2O molecules, the number N of layers building up CSDs, σ^* and σ_z are listed in Table 2.

A similar model was found for pH values of 6.41 and 5.98. This model, which is described in the method section, includes both a periodic structure containing only 2W layers and a MLS containing the three layers types (2W:1W:0W ratio 60:30:10—Figs. 1, 5, 6). The relative abundance of the MLS increases slightly at the expense of the periodic one as pH decreases (Fig. 6). Structure models obtained for the pH values down to 2.88 are quite similar to the previous one, differing only in the presence of a small amount (~2%) of 1W layers in the former periodic structure (Fig. 6). Again, the relative contribution of

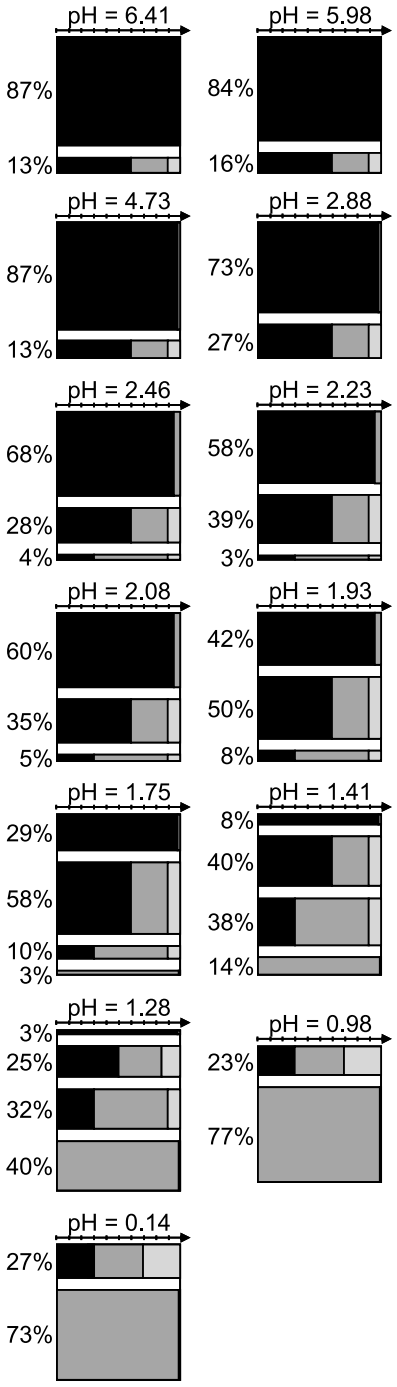

Fig. 6. Structure models obtained from XRD profile modelling for samples prepared under acidic conditions. Symbols and notations as for Figure 1d.

the most homogeneous structure decreases with decreasing pH. For pH values between 2.46 and 1.93, all attempts to reproduce experimental XRD patterns with two contributions were unsuccessful. As the asymmetry on the high angle side of the 001 reflection becomes more pronounced (Figs. 5, 7) it was necessary to introduce a third contribution. As compared to the previous two contributions, this additional MLS must incorporate a noticeable amount of 1W layers to account for the observed asymmetry. The optimum composition determined for this additional MLS was a 2W:1W:0W ratio of 30:60:10 (Figs. 5, 6). In addition, the composition of the mostly bi-hydrated structure was modified to increase the content of 1W layers up to 5% for these pH values between 2.46 and 1.93. The contributions of the different MLS to the XRD pattern recorded for sample pH = 1.93 are illustrated in Figure 7a, in which it is possible to observe the contribution of the additional MLS as a broad modulation at ~14°2θ.

When lowering the pH value to 1.75, it was again necessary to consider an additional contribution to the diffracted intensity to satisfactorily fit the experimental XRD pattern (Figs. 5, 6, 7b). In Figure 7b, the maximum at ~14°2θ now appears as a better-defined peak as compared to Figure 7a, the position of this well-defined maximum indicating that this additional MLS is essentially mono-hydrated. The additional presence of this new MLS (1W:0W ratio 99:1) allows a satisfactory fit to the experimental XRD profile. In Figure 7b, one may also note the presence on the high-angle side of the 001 reflection of broad modulations whose positions are consistent with those of the various MLSs contributing to the calculated intensity. The very heterogeneous structure observed at pH 1.41 (Figs. 6, 7c) was modelled using the same four MLSs as those reported for the previous sample. The composition of these four structures was kept constant for the two samples (pH 1.75 and 1.41), the fit of the experimental profile being achieved by varying the relative proportions of the various MLSs (Figs. 5, 6, 7c). A similar model was used to fit the experimental XRD pattern recorded at pH 1.28 (Figs. 5, 6, 7d). In this model, variation of the relative proportion of the different MLSs accounts for most of the profile modification in addition to a limited decrease of the 2W layer content in one of the MLSs. As for the sample at pH = 1.75, modulations, now observed on the low-angle side of the 001 reflection, allow the composition of the different contributions (Fig. 7d) to be defined. On XRD patterns recorded at pH values of 0.98 and 0.14, the 001 reflection appears sharper and more symmetrical, thus allowing a satisfactory fit with only two contributing MLSs (Figs. 5, 6, 7e). The first MLS accounts for most of the diffracted intensity and corresponds to an almost periodic 1W structure, whereas a second MLS (2W:1W:0W ratio 30:40:30) enables the "tails" of the 001 reflection to be fitted (Figs. 6, 7e). With decreasing pH, the content of 2W layers slightly decreases in the latter MLS (Fig. 6).

While fitting all the XRD patterns collected under acidic conditions, special attention was paid to keep layer thickness constant for all three layer types (2W, 1W, and 0W—Table 2). In addition, for a given sample, the layer and crystal parameters were kept identical for all the MLSs, and only the composition and the relative proportions of the different MLSs was allowed to vary. Most structural parameters were found constant with pH, except for the size of CSDs and σ_z, which decrease with decreasing pH, whereas the water content slightly increases in 1W layers (Table 2). The relative proportions of the different layer types are plotted in Figure 8 as a function of pH to highlight the change in hydration state induced by the progressive exchange of H_3O^+ for interlayer cations as pH decreases.

3.3. Solid Characterisation under Basic Conditions

No significant change in the 001 reflection profile is observed over the basic pH range (Fig. 4b), except for a limited shift of the

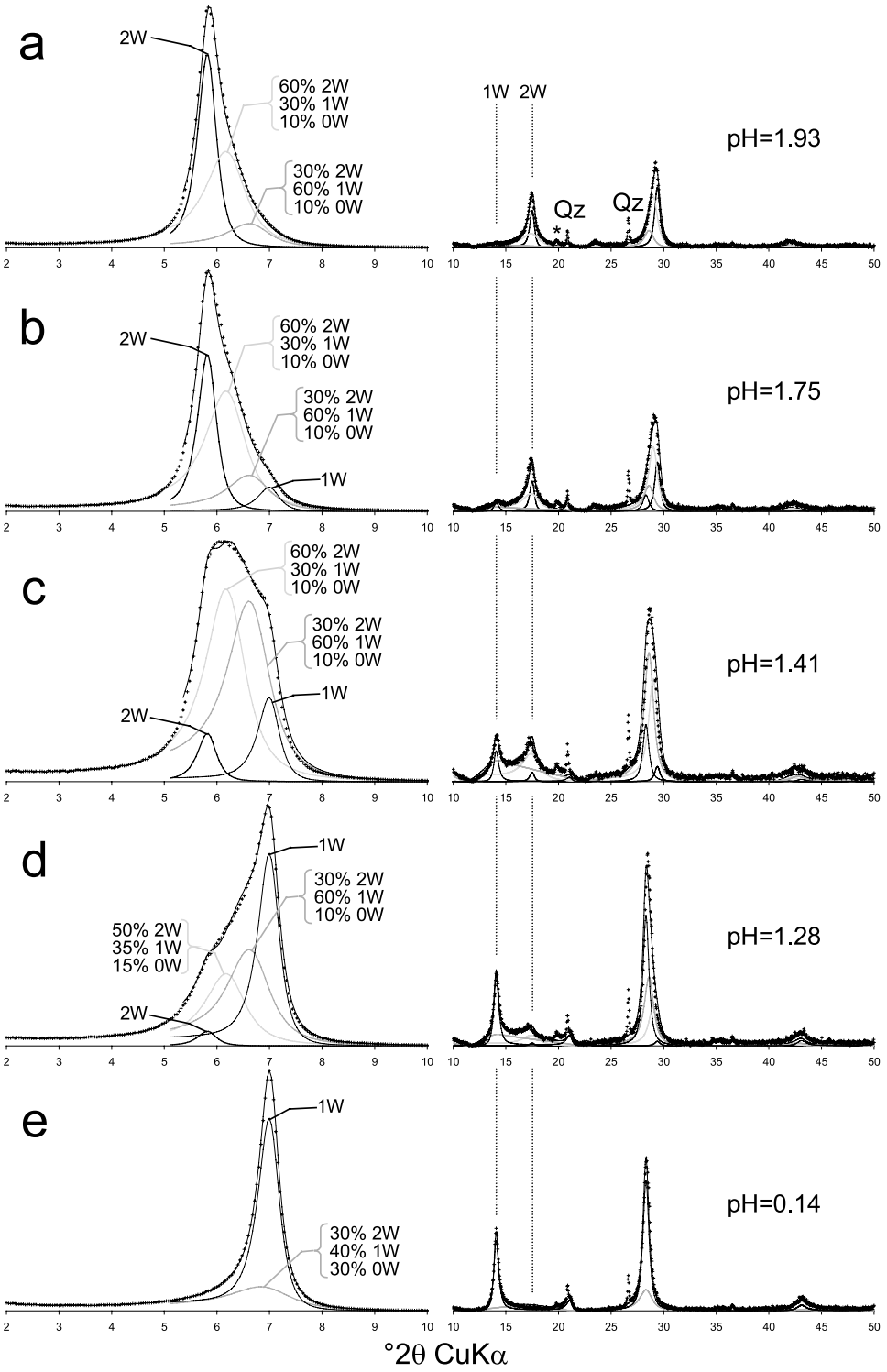

Fig. 7. Respective contributions of the various mixed-layer structures (MLSs) to the calculated profiles. Intensities in the high angle region (10–50°2θ) are enlarged (×10) as compared to the lower angle region (2–10°2θ). The different MLSs are shown as bold, light grey, dark grey and thin sold lines, experimental data are shown as crosses. * indicates hk bands, whereas Qz denotes the presence of accessory quartz reflections. **a)** pH = 1.93. **b)** pH = 1.75. **c)** pH = 1.41. **d)** pH = 1.28. **e)** pH = 0.14.

position from 15.20 Å for near neutral pH conditions to 15.15 Å at pH = 12.62. The extremely similar XRD profiles observed over the whole angular domain (Figs. 4b, 9) are indicative of a constant hydration state over the whole basic pH range. This is confirmed by the comparison between the experimental and calculated XRD patterns (Fig. 9) and by the structure models reported in Figure 10

Table 2. Optimum structure parameters determined from the fitting of XRD profiles recorded for samples prepared under acidic conditions.

pH	LT 2W	LT 1W	LT 0W	N	σ^*	σ_z	nH_2O 2W	nH_2O 1W
6.41	15.18	12.60	10.00	8.7	6.5	0.35	2×3.2	3.2
5.98	15.18	12.60	10.00	8.7	6.3	0.35	2×3.2	3.2
4.73	15.18	12.60	10.00	8.8	6.3	0.35	2×3.2	3.2
2.88	15.18	12.60	10.00	8.9	6.1	0.31	2×3.2	3.2
2.46	15.18	12.60	10.00	8.9	6.0	0.31	2×3.2	3.2
2.23	15.18	12.60	10.00	8.9	6.0	0.30	2×3.2	3.2
2.08	15.18	12.60	10.00	8.9	5.8	0.30	2×3.2	3.2
1.93	15.18	12.60	10.00	8.9	5.8	0.28	2×3.2	3.2
1.75	15.18	12.60	10.00	8.9	5.8	0.26	2×3.2	3.3
1.41	15.18	12.60	10.00	8.9	5.6	0.23	2×3.2	3.3
1.28	15.18	12.60	10.00	9.8	5.6	0.23	2×3.2	3.3
0.98	15.18	12.60	10.00	10.0	6.1	0.23	2×3.2	3.3
0.14	15.18	12.60	10.00	10.0	6.1	0.23	2×3.2	3.3

Note: Layer thickness (LT) of bi-hydrated, mono-hydrated and dehydrated layers (2W, 1W and 0W layers, respectively) are given in Å. For hydrated layers, the amount of interlayer H_2O molecules is given per $O_{20}(OH)_4$. N is the mean number of layers in the coherent scattering domains, while the orientation parameter σ^* and layer thickness variability parameter σ_z are given in ° and in Å, respectively.

and further detailed in Table 3. A model similar to that obtained in near neutral conditions (Fig. 1) was used to reproduce the experimental patterns. This model consists of two structures, the first one containing exclusively (6.41–9.59 pH range) or mostly (11.24–12.62 pH range) 2W layers, whereas the three layer types are present in the second MLS (Fig. 10). The relative proportions of the two structures (Fig. 10) and that of the different layer types (Fig. 8) are about constant over the basic pH range. Most structural parameters were also found to be constant over the basic pH range since only a limited increase in the number of layers in the CSDs and a slight decrease of the layer thickness for 2W layers were observed with increasing pH (Table 3).

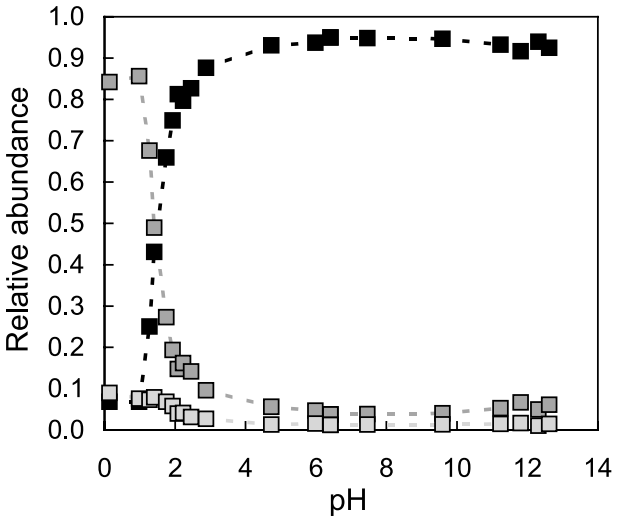

Fig. 8. Relative proportion of the different layer types obtained from XRD profile modelling as a function of pH. Solid squares: 2W layers; dark grey squares: 1W layers; light grey squares: 0W layers.

4. DISCUSSION

4.1. H_3O^+-for-Ca^{2+} Exchange at Low pH

4.1.1. H_3O^+-for-Ca^{2+} exchange. XRD vs. chemical modelling

Under acidic conditions, a dramatic change in the hydration state is observed as pH decreases from the position of the 001 reflection, which shifts from 15.2 Å (2W layers) under near-neutral conditions to 12.6 Å (1W layers) under low pH conditions. As Ca-saturated low-charge montmorillonite is predominantly bi-hydrated at 40% RH, this modification may be linked to the progressive exchange of protons for interlayer Ca^{2+} that can be deduced from the chemical data (Fig. 3). This data can be simulated with the model given by Tournassat et al. (2004a, 2004b) to deduce the interlayer chemical composition as a function of pH (Fig. 11). The cation exchange reaction selectivity coefficients (K_{int}) reported by Tournassat et al. (2004a) were used (Table 1), whereas the structural CEC was adjusted to a consistent 0.94 $eq.kg^{-1}$ value; no other parameter was fitted. Interlayer composition modelling confirms that Na, Al, Fe or Mg do not sorb in the interlayer to a significant extent (data not shown). This chemical modelling rather implies the sorption in the interlayer of several species such as Ca^{2+} or H^+, but also $CaCl^+$ ion pairs. The incorporation of the latter ion pairs at high ionic strength has been demonstrated by Ferrage et al. (2005b) from the resulting modification of XRD reflection intensity distribution and of the layer thickness value. In the present study, no significant change in the reflection relative intensities is observed and the layer thickness value determined for 2W layers is remarkably constant over the whole low-pH range (Fig. 5–Table 2). However, the XRD modelling approach is not sensitive enough to detect the low amount of sorbed $CaCl^+$ species modelled (Fig. 11).

The consistency between the XRD modelling and chemical modelling results can be assessed by calculating the hydration state of the sample from the latter results while assuming a fixed hydration state for each interlayer cation. At near-neutral pH (pH = 6.41), interlayers are purely Ca^{2+}-saturated and the

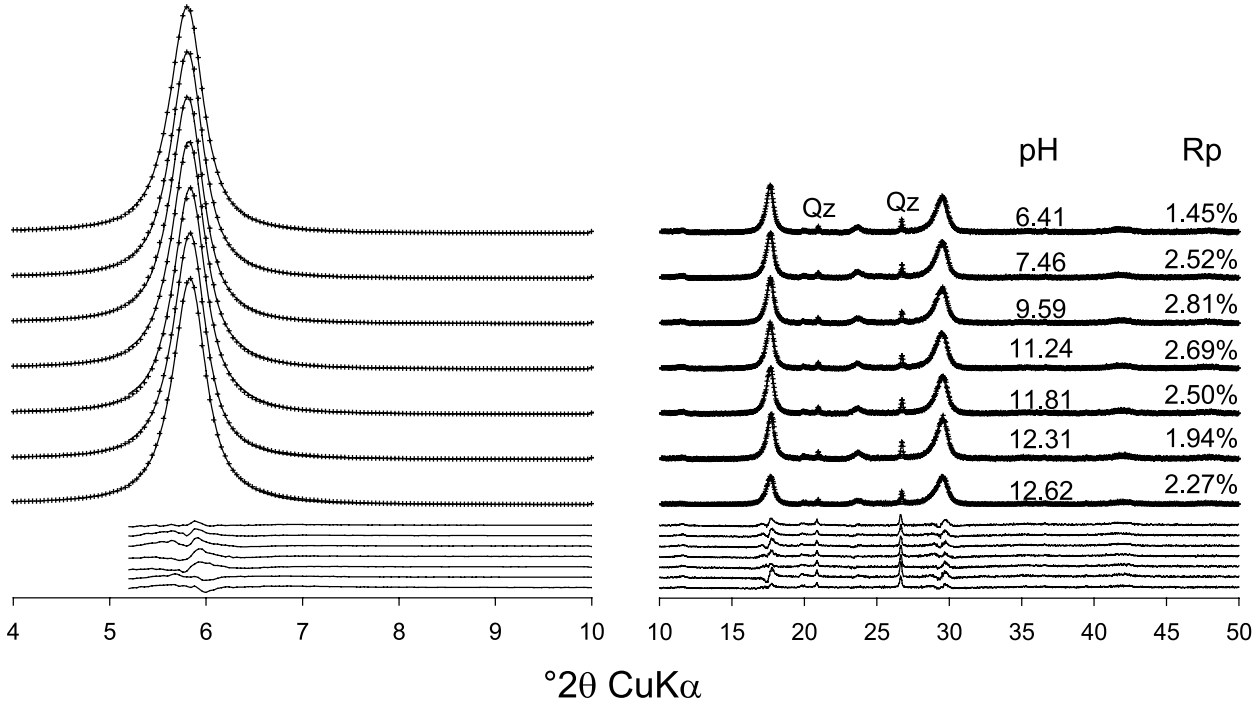

Fig. 9. Comparison between experimental and calculated XRD patterns as a function of pH under alkaline conditions. Symbols as for Figure 5.

hydration state of the sample (2W:1W:0W ratio 95:4:1) determined at this pH may be attributed to Ca^{2+}-saturated layers. At extremely low pH (0.14), the 2W:1W:0W ratio is 6:84:10. However, even at this low pH value, a small proportion of Ca^{2+} cations are still sorbed in the smectite interlayer (0.004 mol.kg^{-1} at pH = 0.14), and the 2W present at this low pH value could possibly be related to remaining Ca^{2+}-saturated layers. H_3O^+-saturated layers were thus assumed to be either 1W or 0W in a 89:11 ratio similar to the 84:10 ratio determined from XRD profile modelling. Using these two hydration states for Ca^{2+}- and H_3O^+-saturated layers it is possible to calculate from the chemical modelling results the proportion of the different layer types as a function of pH (Fig. 12). The excellent agreement found with the data derived from XRD profile modelling confirms that H_3O^+ and Ca^{2+} cations do not coexist in a single interlayer, since this coexistence would induce a significant and strong discrepancy, particularly in the transition region. This segregation of the different cations in different interlayers corresponds to the "demixed state" previously described in heteroionic smectites.

Based on water adsorption isotherms, Glaeser and Méring (1954) first suspected the presence of a demixed state in (Na, Ca)-smectites. They demonstrated that Na^+ and Ca^{2+} cations tend to be distributed in different interlayers but the demixing was interpreted as being incomplete for RH values lower than 75%. These results were confirmed by Levy and Francis (1975) using XRD, and Mamy and Gaultier (1979) reported a similar behaviour in (K, Ca)-smectite. More recently, Iwasaki and Watanabe (1988) were able to refine the distribution of Na^+ and Ca^{2+} cations in smectite and smectite-illite MLSs. Assuming that layers with L.Tck. of ~15.0 Å and ~12.5 Å were Ca- and Na-saturated, respectively, these authors consistently demonstrated that Na^+ and Ca^{2+} cations are distributed in different layers leading to the occurrence of segregated domains.

4.1.2. *Mechanism of H_3O^+-for-Ca^{2+} exchange*

In the observed H_3O^+-for-Ca^{2+} exchange, H_3O^+ cations replace Ca^{2+} cations in a layer-by-layer process, but there is no information on the influence of a given interlayer content on the exchange probability in the next interlayer. The presence of almost periodic 2W and 1W structures systematically suggests a significant segregation in the layer stacking during the exchange process but there is no information directly available on the evolution of the segregation during the process. However, the occurrence probabilities of every layer pair can be calculated from the structure models obtained (Fig. 6—Drits and Tchoubar, 1990), and it is especially relevant to follow the segregation of Ca-saturated 2W layers by using the segregation index Sg(2W) defined by Cesari et al. (1965) and more recently by Drits and Tchoubar (1990):

$$\mathrm{Sg(2W)} = 1 - \frac{1 - P_{2W-2W}}{1 - W_{2W}}, \tag{4}$$

where $W_{2W} < P_{2W-2W} \leq 1$, W_{2W} being the relative abundance of 2W layers in the sample and P_{2W-2W} the probability for a 2W layer to follow a 2W layer in the layer stacks. Sg(2W) ranges from 1 for a physical mixture and 0 for a random distribution of layers. To account for the n structures contributing to the diffracted intensity W_{2W} is expressed as:

$$W_{2W} = \sum_{i=1}^{n} \left[\mathrm{Ab} \,.\, \mathrm{MLS}^i \times W_{2W}^i \right] \tag{5}$$

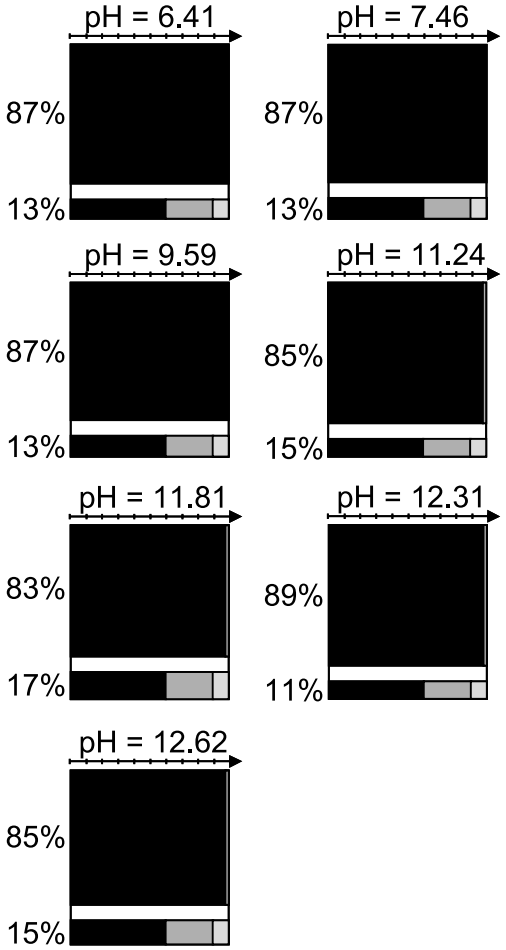

Fig. 10. Structure models obtained from XRD profiles modelling for samples prepared under alkaline conditions. Symbols and notations as for Figure 1d.

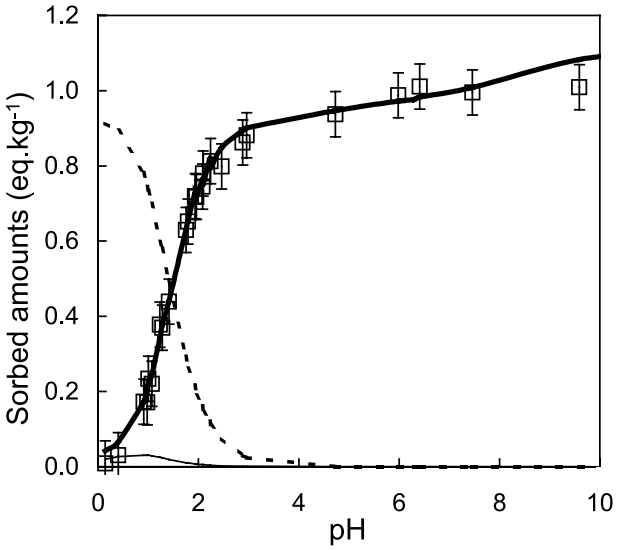

Fig. 11. Apparent amount of Ca sorbed on smectite as a function of pH. Experimentally determined values: open squares. Results of the exchange modelling using the modelling approach developed by Tournassat et al. (2004a) are shown as bold solid lines (Ca^{2+}), dashed lines (H^+), and solid lines ($CaCl^+$).

where Ab.MLS^i is the relative contribution of the structure MLS^i, and W^i_{2W} the relative proportion of 2W layers in this structure. For the global sample P_{2W-2W} is calculated as:

$$P_{2W-2W} = \frac{W_{2W-2W}}{W_{2W}} \quad (6)$$

where W_{2W-2W} is the relative abundance of layer pairs constituted of two 2W layers. Taking into account the n structures contributing to the diffracted intensity, this term is calculated as:

$$W_{2W-2W} = \sum_{i=1}^{n} \left[Ab\,.\,MLS^i \times W^i_{2W-2W} \right] \quad (7)$$

In the present study, layer stacking is random in all MLS contributing to the diffracted intensity and Eqn. 4 can thus be transformed to:

$$Sg(2W) = 1 - \frac{1 - \sum_{i=1}^{n} \left[Ab\,.\,MLS^i \times \left(W^i_{2W}\right)^2 \right] / \sum_{i=1}^{n} \left[Ab\,.\,MLS^i \times W^i_{2W} \right]}{1 - \sum_{i=1}^{n} \left[Ab\,.\,MLS^i \times W^i_{2W} \right]}, \quad (8)$$

Note that Eqn. 8 is valid only if all MLS contributing to the diffracted intensity are randomly interstratified. As a function of pH, the calculated Sg(2W) value ranges from 0.2 to 0.4 whatever the W_{2W} value (Fig. 13). This Sg(2W) value corre-

Table 3. Optimum structure parameters determined from the fitting of XRD profiles recorded for samples prepared under alkaline conditions.

pH	LT 2W	LT 1W	LT 0W	N	σ^*	σ_z	nH_2O 2W	nH_2O 1W
6.41	15.18	12.60	10.00	8.7	6.5	0.35	2×3.2	3.2
7.46	15.17	12.60	10.00	9.0	6.5	0.35	2×3.2	3.2
9.59	15.17	12.60	10.00	9.0	6.5	0.35	2×3.2	3.2
11.24	15.16	12.60	10.00	9.1	6.5	0.35	2×3.2	3.2
11.81	15.15	12.60	10.00	9.4	6.0	0.35	2×3.2	3.2
12.31	15.15	12.60	10.00	9.4	5.5	0.35	2×3.2	3.2
12.62	15.15	12.60	10.00	9.3	5.0	0.35	2×3.2	3.2

Note: Layer thickness (LT) of bi-hydrated, mono-hydrated and dehydrated layers (2W, 1W and 0W layers, respectively) are given in Å. For hydrated layers, the amount of interlayer H_2O molecules is indicated per $O_{20}(OH)_4$. N is the mean number of layers in the coherent scattering domains, while the orientation parameter σ^* and layer thickness variability parameter σ_z are given in ° and in Å, respectively.

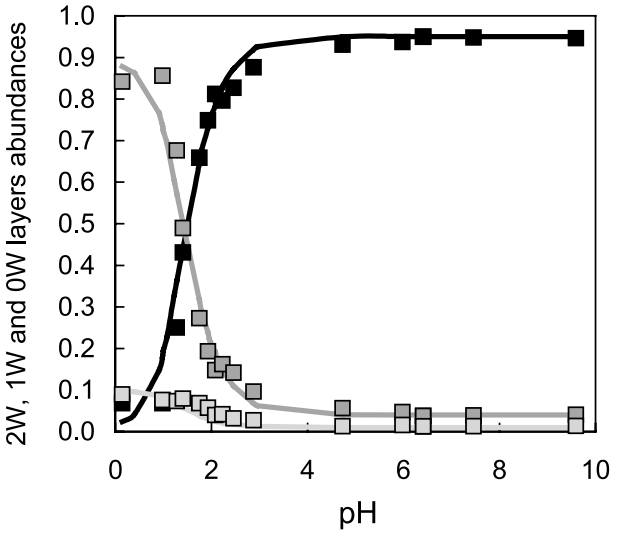

Fig. 12. Comparison between the relative abundance of the different layer types obtained from XRD profile modelling (symbols) and that derived from chemical modelling (solid lines), as a function of pH. Light grey, dark grey and black colours correspond to 0W, 1W, and 2W layers, respectively.

sponds to a limited degree of segregation, and its stability, within error, throughout the whole pH range, including the H_3O^+-for-Ca^{2+} exchange zone, indicates that this cation exchange occurs randomly within the crystals with no influence of the interlayer cation present in the adjacent interlayers.

4.1.3. XRD Characterisation of the resulting solid

The XRD profile modelling approach used in the present study allowed all of the experimental patterns to be reproduced satisfactorily, but it led in a few cases to extremely heterogeneous structures, as up to four contributions were sometimes necessary to fit XRD profiles. However, to reduce the number

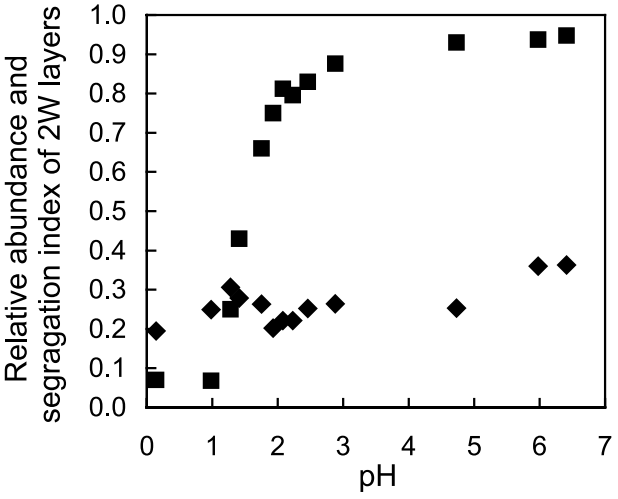

Fig. 13. Relative abundance of 2W layers obtained from XRD profile modelling (solid squares) and segregation index of 2W layers (Sg(2W) – solid diamonds) as a function of pH under acidic conditions.

of adjustable parameters associated with these additional contributions, all layers were assumed to have strictly identical properties (layer thickness, σ_z, and H_2O content) in all contributions for a given sample. In addition, the size of the CSDs (N) and the preferred orientation parameter (σ^*) were also identical for the different MLSs contributing to a given XRD pattern. At each pH value, adjustable parameters were thus limited to the composition of the different MLSs, and to their relative proportions. Moreover, when four MLSs were used to fit the experimental XRD patterns (pH = 1.75, 1.48 and 1.28 — Fig. 6), these parameters were found to be consistent from one pH value to the next. Two of these four contributions correspond to essentially bi- or mono-hydrated smectite whereas the other two, which account for the heterogeneous layer stacks resulting from the ongoing exchange process, have approximately constant compositions.

The decrease in interlayer thickness fluctuation (σ_z parameter) from 0.35 Å for near neutral conditions to 0.23 Å (Table 2) for acidic conditions is associated with the hydration state modification from an essentially bi-hydrated state to an essentially mono-hydrated state. This correlation is consistent with the observations of Ferrage et al. (2005a) on a montmorillonite SWy-1 sample saturated with various monovalent and divalent cations. Indeed, these authors noted that the σ_z parameter is significantly higher (0.25–0.50 Å) when the sample is dominated by 2W layers than when 0W or 1W layers prevail (0.15–0.25 Å). They attributed the higher σ_z values determined for 2W layers to their higher layer thickness, which implies in turn weaker electrostatic interactions between the negatively charged layer and the interlayer cations. As a consequence, the respective positions of two adjacent 2:1 layers are weakly constrained and the resulting variation of layer thickness from one interlayer to the adjacent one is enlarged. This phenomenon is likely to occur also for 1W layers, but the lower layer thickness values and the different location of H_2O molecules considerably reduce the screening of electrostatic interactions between the 2:1 layer and the interlayer cations.

In addition, Ferrage et al. (2005a) have observed higher σ_z values at the transition between two individual hydration states, possibly as a result of the coexistence, within a single interlayer, of different hydration states resulting in a high degree of fluctuation in the interlayer thickness. On the contrary, in the present study, the σ_z values steadily decrease with decreasing pH even over the H_3O^+-for-Ca^{2+} exchange zone characterised by heterogeneous structures. Such an even decrease is indicative of the homogeneous hydration state of each interlayer, that is of the mutual exclusion of Ca^{2+} and H_3O^+ cations in a single interlayer, again suggesting a layer-by-layer exchange process leading to a "demixed" state (Glaeser and Méring, 1954; Levy and Francis, 1975; Mamy and Gaultier, 1979; Iwasaki and Watanabe, 1988). This is also consistent with the constant layer thickness values determined for both 1W and 2W layers throughout the low-pH range (Table 2).

In addition, the number of layers in the CSDS also increases from ~8.7 under neutral conditions to ~10.0 under acidic conditions. This steady increase with the transition from a bi-hydrated state to a mono-hydrated state is consistent with the decreasing N values determined by Ferrage et al. (2005a) for smectite XRD at high RH values when 2W layers prevail, in agreement with Mystkowski et al. (2000). This evolution can

possibly be related to the breakdown of crystals resulting from the swelling of specific interlayers, which statistically decreases the crystallite thickness with increasing RH.

4.2. Assessment of the Presence of $CaOH^+$ Ion Pairs in the Alkaline pH Range

The possibility of interlayer $CaOH^+$ ion pairs compensating the octahedral charge under alkaline conditions has been evoked on the basis of cation exchange experiments and chemical modelling to model the apparent increase of sorbed Ca^{2+} at high pH values (Fig. 3—Charlet and Tournassat, 2005; Tournassat et al., 2004a, 2004b). However, Ferrage et al. (2005b) has shown that the presence of $CaCl^+$ ion pairs similarly evoked for samples equilibrated with saline solutions (Sposito et al., 1983a, 1983b; Tournassat et al., 2004b) induces significant modification of the experimental XRD patterns. These modifications affect (i) the intensity ratio between the reflections, as a result of the increase in the electronic density in the interlayer; (ii) the homogeneity of layer thickness (lower σ_z values); and (iii) the hydration properties of exchanged smectite, in particular by lowering the relative humidity value necessary for the bi- to mono-hydrated transition. In addition, the presence of $CaCl^+$ ion pairs may be assessed using NIR-DR spectroscopy from its influence on interlayer H_2O vibration bands. The methodology developed by Ferrage et al. (2005b) to assess the presence of $CaCl^+$ ion pairs in the interlayer of montmorillonite, was applied in the present study to assess the possible presence of $CaOH^+$ ion pairs under high pH conditions.

4.2.1. XRD characterisation of the solid

Under alkaline conditions, no significant modification of the experimental XRD patterns is observed as a function of pH and the resulting structure models are similar over the whole pH range investigated (pH 6.41–12.62). However, it was not possible to keep the layer thickness of 2W layers constant and a very limited variation was observed (from 15.17 to 15.15 Å), whereas other structural parameters (σ^*, σ_z, N or water content) were found to be constant over the whole pH range (Table 3). If $CaOH^+$ ion pairs were sorbed in the smectite interlayers at high pH values, relative reflection intensities in the high-angle region would be significantly affected, even though the electron density is lower for $CaOH^+$ ion pairs (28e^-/c.u.) than for $CaCl^+$ ion pairs (36 e^-/c.u.). The impact of $CaOH^+$ ion pairs on XRD profiles is illustrated in Figure 14, which shows two patterns calculated for the sample at pH = 12.62. The first pattern (solid line) is calculated assuming only Ca^{2+} as the interlayer cation, whereas the second pattern (grey line) is calculated with $CaOH^+$ ion pairs as compensating species, all other structure parameters being kept constant. The presence of $CaOH^+$ ion pairs is clearly demonstrated by the increase in the 002 and 003 reflection intensity. On the contrary, all experimental profiles displayed in Figure 9 are similar, and the presence of interlayer $CaOH^+$ ion pairs may be dismissed.

4.2.2. NIR-DR spectroscopy characterisation of the solid

NIR-DR spectroscopy was used as an independent, complementary technique to investigate the possibility of $CaOH^+$ sorption in montmorillonite interlayer under high-pH conditions. This technique allows the amount of water and its local interaction with interlayer species to be studied. In addition, the high sensitivity of infrared spectroscopy for hydroxyls should allow the detection of partial $CaOH^+$-for-Ca^{2+} exchange, especially in the hydroxyl band region. In their study, Ferrage et al. (2005b) showed that when the octahedral charge is compensated by $CaCl^+$ ion pairs instead of Ca^{2+} cations, the main modifications to NIR-DR spectra are: (i) for hydrated samples (40% RH), an increased amount of H_2O induced by the increased amount of interlayer cationic species; and (ii) for out-gassed samples, a shift of H_2O vibration bands induced by the perturbation of the residual H_2O-Ca^{2+} interaction by Cl^- anions. On the contrary, the NIR-DR spectra recorded at 0% and ~40% RH for samples obtained at pH 6.41 and 12.62 (Figs. 15 and 16, respectively) are almost identical to each other, whatever the data collection conditions. In the spectral domain of combinations of H_2O molecules (4550–5500 cm^{-1}), the band at 5240–5250 cm^{-1} can be assigned to H_2O molecules perturbed by interlayer cations. At 0% RH, this band

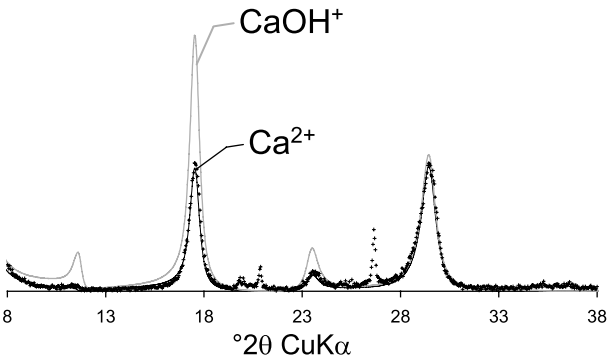

Fig. 14. Comparison between the experimental pattern of the sample prepared at pH = 12.62 (crosses) with those calculated considering Ca^{2+} cations (solid line) or $CaOH^+$ ion pairs (solid grey line) as the sole charge compensating species. Calculated XRD patterns were normalized to the 001 reflection of the experimental XRD pattern at ~15.2 Å (not shown).

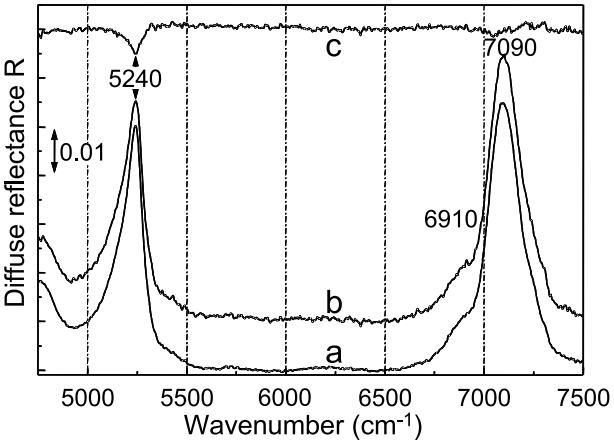

Fig. 15. NIR-DR spectra of out-gassed samples. **a)** Sample prepared under near-neutral conditions (pH = 6.41). **b)** Sample prepared under alkaline conditions (pH = 12.62). **c)** Difference between the above two spectra (c = b − a).

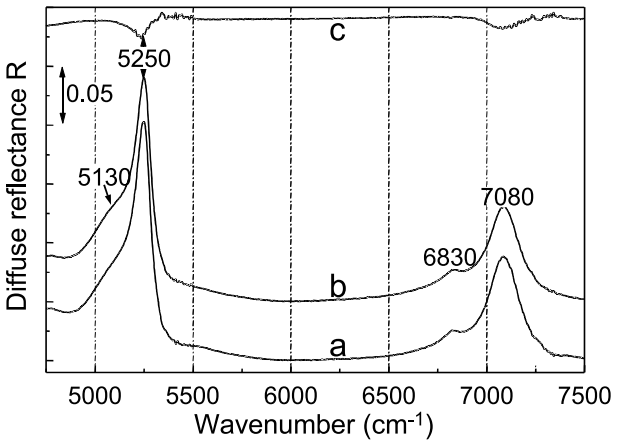

Fig. 16. NIR-DR spectra of hydrated samples (RH = 40 ± 5%). **a)** Sample prepared under near-neutral conditions (pH = 6.41). **b)** Sample prepared under alkaline conditions (pH = 12.62). **c)** Difference between the above two spectra (c = b − a).

is still visible, indicating the presence of H_2O molecules despite the out-gassing conditions (Fig. 15). The residual difference between the spectra recorded for samples obtained at pH 6.41 and 12.62 (Fig. 15c) reveals a slightly higher amount of H_2O molecules in the sample at pH = 6.41. This difference, which probably results from not strictly identical out-gassing conditions and H_2O desorption kinetics for the two experiments, again pleads against the presence of $CaOH^+$ ion pairs in the smectite interlayer under high-pH conditions. In the spectral domain of overtones (6500–7500 cm^{-1}), similar bands are observed for the two samples at 6910 and 7090 cm^{-1}.

As observed under out-gassed conditions, the two spectra recorded at 40% RH for the same samples are similar (Fig. 16), whereas several modifications between the two sets of spectra result from the presence of H_2O molecules. At 40% RH, a shoulder located at ~5130 cm^{-1} is observed for the two samples in the region of combinations (Fig. 16a, 16b) and the band observed at 5240 cm^{-1} under out-gassed conditions is shifted to 5250 cm^{-1}. These two bands account for the presence of H_2O molecules weakly adsorbed on interlayer cations and H-bonded vibrations. Overtones of H_2O molecules and hydroxyl stretching are also shifted by the presence of water and are observed at 6830 and 7080 cm^{-1} for the two hydrated samples. As for spectra recorded under out-gassed conditions, the difference between the two spectra (Fig. 16c) reveals that the amount of H_2O is again slightly higher in the sample prepared at pH = 6.41 as compared to the one obtained under high-pH conditions. This difference most probably results from slightly different experimental conditions rather than from a contrasting interlayer composition, again pleading against the presence of $CaOH^+$ ion pairs in the smectite interlayer under high-pH conditions.

4.2.3. *Implications on the modelling of the analytical chemistry results for the alkaline pH range*

As discussed above, XRD and NIR-DR spectroscopy results consistently show that $CaOH^+$ ion pairs do not enter smectite interlayers at high pH in a calcium cation background. Hence, the analytical chemistry results need to be modelled without the contribution of such ion pairs and the modelling results from Tournassat et al. (2004b), accounting for the sorption of $CaOH^+$ pairs, must be re-examined.

Ca-CEC, the apparent CEC in a Ca^{2+} cation background (in $eq.kg^{-1}$ or $mol_c.kg^{-1}$), is given by the following equation:

$$\text{Ca} - \text{CEC} \Leftrightarrow 2 \times \text{Ca}_{\text{sorbed}} \tag{9}$$

where Ca_{sorbed} is the amount of Ca sorbed on clay surfaces in $mol.kg^{-1}$. If one assumes that $CaOH^+$ is the only compensating species in smectite interlayers at high pH, the reaction taking place during the Ca-CEC measurement experiment is:

$$\text{XCaOH} + \text{NH}_4^+ \Leftrightarrow \text{XNH}_4 + \text{Ca}^{2+} + \text{OH}^- \tag{10}$$

where X^- represents one mole of the exchanger phase. Then, $Ca_{sorbed} = 2\,[Ca^{2+}]_1/\rho$, where $[Ca^{2+}]_1$ is the concentration of Ca^{2+} released in solution by reaction 10 and determined experimentally (Sposito et al., 1981, 1983a). The presence of $CaOH^+$ in exchange position thus leads to an apparent increase in the Ca-CEC as each Ca in solution is converted to two structural charges in the calculation, even though one $CaOH^+$ equilibrates only one structural charge (Sposito et al., 1983a, 1983b).

$CaOH^+$ exchange also leads to the net consumption of one OH^- per sorbed $CaOH^+$, leading to a one-to-one correlation between the change of apparent surface charge (disappearance of OH^- in $eq.kg^{-1}$) and that of Ca-CEC (in $eq.kg^{-1}$—reaction 11—Tournassat et al., 2004a, 2004b):

$$\text{X}_2\text{Ca} + 2\,\text{OH}^- \Leftrightarrow 2\,\text{XCaOH} \tag{11}$$

Hence, reaction 11 could explain almost perfectly the increase in Ca-CEC as a function of pH in the present study and the Ca^{2+}-CEC vs. "sorbed" OH^- stoichiometry observed in the study of Tournassat et al. (2004a, 2004b). This assumption is in contradiction with the experimental evidence deduced from XRD and NIR-DR spectroscopy results.

As precipitation of a Ca-Si phase can be an alternative explanation for the apparent increase in Ca sorption and for the decrease in Si concentration occurring under high-pH conditions, the saturation index of many Calcium-Silicate-Hydrate (CSH—Hatches, 2000) were calculated as a function of pH for the solution composition reported in the present study and in that of Tournassat et al. (2004a). Among the results listed in Table 4, it is possible to note that both CSH 0.8 and CSH 1.1 (Hatches, 1998) are oversaturated with respect to the chemical conditions prevailing in solution. Since CSH 0.8 is closer from its equilibrium ion activity product than CSH 1.1, the former phase is more likely to precipitate, as described in the following reaction:

$$0.8\,\text{Ca}^{2+} + \text{SiO}_2 + 1.4\,\text{H}_2\text{O} + 1.6\,\text{OH}^- \Leftrightarrow \text{Ca}_{0.8}\text{SiO}_5\text{H}_{4.4} \tag{12}$$

The precipitate would remain in the clay slurry during the centrifugation step before addition of NH_4^+. This addition desorbs Ca^{2+} from the interlayer and also induces the dissolution of the CSH 0.8 phase as a result of the pH decrease resulting from the dilution of the alkaline solution in contact with the clay slurry. In turn, this dissolution leads to the release

Table 4. Saturation index (SI) calculated for two CSH phases as a function of pH. Ca and Si concentration conditions measured in the present study and in that of Tournassat et al. (2004a) have been used.

pH	[Ca] (mmol.L^{-1})	[Si] (mmol.L^{-1})	log SI CSH 0.8	log SI CSH 1.1
		This study		
11.81	2.18	0.221	0.0	0.6
12.31	6.23	0.100	0.1	1.1
12.62	13.57	0.020	−0.4	0.9
		Tournassat et al. (2004a) study		
11.38	5.61	0.68	0.5	1.0
11.93	4.41	0.25	0.3	1.0
10.77	50.8	0.22	0.2	0.5
11.16	50.1	0.14	0.2	0.7

of Ca^{2+} in solution and to the observed apparent increase in the Ca-CEC. Since reaction 12 leads to a one-to-one correlation between the change of apparent surface charge and that of Ca-CEC (disappearance of 1.6 mol_c of OH^- and $0.8 \times 2 = 1.6$ mol_c of Ca^{2+}), it may equally account for the observed Ca^{2+}-CEC vs. "sorbed" OH^- stoichiometry.

5. CONCLUSIONS

The present study focuses on the modification to the hydration state occurring in Ca-SWy-2 montmorillonite as a function of pH. Under acidic conditions, a transition from bi-hydrated to mono-hydrated state was observed, occurring as the result of a H_3O^+-for-Ca^{2+} exchange in the smectite interlayer. XRD profile modelling was successfully applied to determine the proportion of the different layer types in the reacted samples, even for extremely heterogeneous hydration states. The proportion of layers obtained was consistent with that derived from chemical modelling, confirming the latter results and demonstrate the ability of these two independent methods to accurately characterise chemical/structural modifications in smectite interlayers. In addition, the exchange between Ca^{2+} cations and H_3O^+ ions has been shown to occur as a layer-by-layer process, taking place randomly in the layer stack.

Under high-pH conditions, the possible presence of $CaOH^+$ ion pairs in the smectite interlayer is proven to be false from results obtained both by XRD profile modelling and by NIR-DR spectroscopy. As a consequence, the apparent increase in Ca sorption and the decrease in Si concentration occurring under high-pH conditions probably result most likely from the precipitation of a CSH phase, which is thermodynamically favoured.

Acknowledgments—The results presented in the present article were collected during a Ph.D. thesis granted by ANDRA (French National Agency for Nuclear Waste Disposal). ANDRA is thanked for its permission to publish this manuscript, and the authors acknowledge its financial support. The French Geological Survey (BRGM) is acknowledged for its editorial financial support. EF is grateful to Pr. Boris A. Sakharov for fruitful discussions during XRD profile modelling. The manuscript was improved by the constructive reviews of two anonymous reviewers and AE Garrison Sposito, and by the remarks of Emmanuel Jacquot on an early version of the manuscript.

Associate editor: G. Sposito

REFERENCES

Appelo C. A. J. and Postma D. (2000) Geochemistry, Groundwater and Pollution. Rotterdam press, 536pp.

Baeyens B. and Bradbury M. H. (1997) A mechanistic description of Ni and Zn sorption on Na-montmorillonite. Part I: Titration and sorption measurements. *J. Contam. Hydrol.* **27,** 199–222.

Bérend I., Cases J. M., François M., Uriot J. P., Michot L. J., Masion A. and Thomas F. (1995) Mechanism of adsorption and desorption of water vapour by homoionic montmorillonites: 2. the Li^+, Na^+, K^+, Rb^+ and Cs^+ exchanged forms. *Clays Clay Miner.* **43,** 324–336.

Bishop J., Murad E. and Dyar M. D. (2002) The influence of octahedral and tetrahedral cation substitution on the structure of smectites and serpentines as observed through infrared spectroscopy. *Clay Miner.* **37,** 361–628.

Bradbury M. H. and Baeyens B. (1997) A mechanistic description of Ni and Zn sorption on Na-montmorillonite. Part II: modeling. *J. Contam. Hydrol.* **27,** 223–248.

Bradley W. F., Grim R. E. and Clark G. F. (1937) A study of the behavior of montmorillonite on wetting. *Z. Kristallogr.* **97,** 260–270.

Burneau A., Barrès O., Gallas J. P. and Lavalley J. C. (1990) Comparative study of the surface hydroxyl groups of fumed and precipitated silicas. 2. Characterization by infrared spectroscopy of the interaction with water. *Langmuir* **6,** 1364–1372.

Burneau A. and Carteret C. (2000) Near infrared and ab initio study of the vibrational modes of isolated silanol on silica. *Phys. Chem. Chem. Phys.* **2,** 3217–3226.

Cases J. M., Bérend I., François M., Uriot J. P., Michot L. J. and Thomas F. (1997) Mechanism of adsorption and desorption of water vapour by homoionic montmorillonite: 3. the Mg^{2+}, Ca^{2+}, Sr^{2+} and Ba^{2+} exchanged forms. *Clays Clay Miner.* **45,** 8–22.

Cesari M., Morelli G. L. and Favretto L. (1965) The determination of the type of stacking in mixed-layer clay minerals. *Acta Cryst.* **18,** 189–196.

Charlet L. and Tournassat C. (2005) Fe(II)-Na(I)-Ca(II) cation exchange on montmorillonite in chloride medium; evidence for preferential clay adsorption of chloride—metal ion pairs in seawater. *Aquat. Geochem.* (in press).

Claret F., Bauer A., Schafer T., Griffault L. and Lanson B. (2002) Experimental Investigation of the interaction of clays with high-pH solutions: a case study from the Callovo-Oxfordian formation, Meuse-Haute Marne underground laboratory (France). *Clays Clay Miner.* **50,** 633–646.

Cuadros J. (1997) Interlayer cation effects on the hydration state of smectite. *Am. J. Sci.* **297,** 829–841.

Delville A. (1991) Modeling the clay-water interface. *Langmuir* **7,** 547–555.

Drits V. A. and Sakharov B. A. (1976) X-Ray structure analysis of mixed-layer minerals. Dokl. Akad. Nauk SSSR, Moscow, 256 pp.

Drits V. A. and Tchoubar C. (1990) X-ray diffraction by disordered lamellar structures: Theory and applications to microdivided silicates and carbons. Springer-Verlag, Berlin, 371 pp.

Drits V. A., Sakharov B. A., Lindgreen H. and Salyn A. (1997a) Sequential structure transformation of illite-smectite-vermiculite during diagenesis of Upper Jurassic shales from the North Sea and Denmark. *Clay Miner.* **32,** 351–371.

Drits V. A., Srodon J. and Eberl D. D. (1997b) XRD measurement of mean crystallite thickness of illite and illite/smectite: reappraisal of the kubler index and the scherrer equation. *Clays Clay Miner.* **45,** 461–475.

Elprince A. M., Vanselow A. P. and Sposito G. (1980) Heterovalent, ternary cation exchange equilibria: NH^{4+}-Ba^{2+}-La^{3+} exchange on montmorillonite. *Soil Sci. Soc. Am. J.* **44,** 964–969.

Ferrage, E., Lanson, B., Sakharov, B.A. and Drits, V.A (2005a) Investigation of smectite hydration properties by modeling of X-ray diffraction profiles. Part 1. Montmorillonite hydration properties. *Am. Mineral.* (in press).

Ferrage, E., Tournassat, C., Rinnert, E., Charlet, L. and Lanson, B (2005b) Experimental evidence for calcium-chloride ion pairs in the interlayer of montmorillonite. A XRD profile modelling approach. *Clays Clay Miner.* (in press).

Fletcher P. and Sposito G. (1989) The chemical modeling of clay/electrolyte interactions for montmorillonite. *Clay Miner.* **24,** 375–391.

Gilbert M. and Laudelout H. (1965) Exchange properties of hydrogen ions in clays. *Soil Sci.* **100,** 159–162.

Glaeser R. and Méring J. (1954) Isothermes d'hydratation des montmorillonites bi-ioniques (Ca, Na). *Clay Mineral. Bull.* **2,** 188–193.

Guinier A. (1964) Théorie et technique de la radiocristallographie. Dunod, Paris, 740 pp.

Hatches (2000) HATCHES, Harwell/Nirex thermodynamic database for chemical equilibrium studies. Version NEA13 available at http://www.nea.fr/abs/html/nea-1310.html#10.

Howard S.A. and Preston K.D. (1989) Profile fitting of powder diffraction patterns. In *Modern Powder Diffraction* (eds. D. L. Bish and J. E. Post). Rev. in Mineralogy 20, pp. 217–275 Mineralogical Society of America, Washington D.C.

Iwasaki T. and Watanabe T. (1988) Distribution of Ca and Na ions in dioctahedral smectites and interstratified dioctahedral mica/smectites. *Clays Clay Miner.* **36,** 73–82.

Kittrick J. A. (1969a) Interlayer forces in montmorillonite and vermiculite. *Soil Sci. Soc. Am. J.* **33,** 217–222.

Kittrick J. A. (1969b) Quantitative evaluation of the strong-force model for expansion and contraction of vermiculite. *Soil Sci. Soc. Am. J.* **33,** 222–225.

Laird D. A. (1996) Model for crystalline swelling of 2:1 phyllosilicates. *Clays Clay Miner.* **44,** 553–559.

Laird D. A. (1999) Layer charge influences ont the hydratation of expandle 2:1 phyllosilicates. *Clays Clay Miner.* **47,** 630–636.

Levy R. and Francis C. W. (1975) Demixing of sodium and calcium ions in montmorillonite crystallites. *Clays Clay Miner.* **23,** 475–476.

Madejova J., Bujdak J., Petit S. and Komadel P. (2000a) Effects of chemical composition and temperature of heating on the infrared spectra of Li-saturated dioctahedral smectites. (I) Mid-infrared region. *Clay Miner.* **35,** 739–751.

Madejova J., Bujdak J., Petit S. and Komadel P. (2000b) Effects of chemical composition and temperature of heating on the infrared spectra of Li-saturated dioctahedral smectites. (II) Near-infrared region. *Clay Miner.* **35,** 753–761.

Mamy J. and Gaultier J. P. (1979) Etude comparée de l'évolution des montmorillonites biioniques K-Ca de Camp-Berteaux et du Wyoming sous l'effet des cycles d'humectation et de dessication. *Clay Miner.* **14,** 181–192.

Méring J. (1949) L'interférence des rayons-X dans les systèmes à stratification désordonnée. *Acta Cryst.* **2,** 371–377.

Mermut A. R. and Lagaly G. (2001) Baseline studies of the clay minerals society source clays: layer-charge determination and characteristics of those minerals containing 2:1 layers. *Clays Clay Miner.* **49,** 393–397.

Mooney R. W., Keenan A. G. and Wood L. A. (1952) Adsorption of water vapor by montmorillonite. II. Effect of exchangeable ions and lattice swelling as measured by X-ray diffraction. *J. Am. Chem. Soc.* **74,** 1331–1374.

Moore D. M. and Reynolds R. C. Jr. (1997) X-ray Diffraction and the Identification and Analysis of Clay Minerals. Oxford University Press, Oxford and New York, 322 pp.

Mystkowski K., Srodon J. and Elsass F. (2000) Mean thickness and thickness distribution of smectite crystallites. *Clay Miner.* **35,** 545–557.

Nagelschmidt G. (1936) The structure of montmorillonite. *Z. Kristallogr.* **93,** 481–487.

Norrish K. (1954) The swelling of montmorillonite. *Disc. Farad. Soc.* **18,** 120–134.

Parkhurst D. L. and Appelo C.A.J (1999) Phreeqc2 user's manual and program U.S. Geological Survey.

Plançon A. (2002) New modeling of X-ray diffraction by disordered lamellar structures, such as phyllosilicates. *Amer. Mineral.* **87,** 1672–1677.

Sakharov B. A. and Drits V. A. (1973) Mixed-layer kaolinte-montmorillonite: a comparison observed and calculated diffraction patterns. *Clays Clay Miner.* **21,** 15–17.

Sakharov B. A., Lindgreen H., Salyn A. and Drits V. A. (1999) Determination of illite-smectite structures using multispecimen X-Ray diffraction profile fitting. *Clays Clay Miner.* **47,** 555–566.

Shainberg I., Oster J. D. and Wood J. D. (1980) Sodium/calcium exchange in montmorillonite and Illite suspension. *Soil Sci. Soc. Am. J.* **44,** 960–964.

Shu-Yuan C. and Sposito G. (1981) The thermodynamics of ternary cation exchange systems and the subregular model. *Soil Sci. Soc. Am. J.* **45,** 1084–1089.

Sposito G. (1977) The Gapon and Vanselow selectivity coefficients. *Soil Sci. Soc. Am. J.* **41,** 1205–1206.

Sposito G. (1981) The thermodynamics of soil solution. Oxford University Press, New York.

Sposito G. (1984) Surface chemistry of soils. Oxford University press, New York, 223 pp.

Sposito G., Holtzclaw K. M., Johnston C. T. and Le Vesque C. S. (1981) Thermodynamics of sodium-copper exchange on Wyoming bentonite at 298 K. *Soil Sci. Soc. Am. J.* **45,** 1079–1084.

Sposito G., Holtzclaw K. M., Charlet L., Jouany C. and Page A. L. (1983a) Sodium-calcium and sodium-magnesium exchange on Wyoming bentonite in perchlorate and chloride background ionic media. *Soil Sci. Soc. Am. J.* **47,** 51–56.

Sposito G., Holtzclaw K. M., Jouany C. and Charlet L. (1983b) Cation selectivity in sodium-calcium, sodium-magnesium and calcium-magnesium exchange on Wyoming bentonite at 298 K. *Soil Sci. Soc. Am. J.* **47,** 917–921.

Sposito G., Skipper N. T., Sutton R., Park S. and Soper A. K. (1999) Surface geochemistry of the clay minerals. *Proc. Natl. Acad. Sci. U.S.A.* **96,** 3358–3364.

Stucki J. W., Golden D. C. and Roth C. B. (1984) Effects of reduction and reoxidation of structural iron on the surface charge dissolution of dioctahedral smectites. *Clays Clay Miner.* **32,** 350–356.

Tournassat C., Neaman A., Villiéras F., Bosbach D. and Charlet L. (2003) Nanomorphology of montmorillonite particles: Estimation of the clay edge sorption site density by low-pressure gas adsorption and AFM observations. *Amer. Mineral.* **88,** 1989–1995.

Tournassat C., Greneche J. M., Tisserand D. and Charlet L. (2004a) The titration of clay minerals. Part I. Discontinuous backtitration technique combined to CEC measurements. *J. Coll. Interf. Sci.* **273,** 224–233.

Tournassat C., Ferrage E., Poinsignon C. and Charlet L. (2004b) The titration of clay minerals. Part II. Structural-based model and implications for clay reactivity. *J. Coll. Interf. Sci.* **273,** 234–246.

Van Olphen H. (1965) Thermodynamics of interlayer adsorption of water in clays. *J. Colloid Interf. Sci.* **20,** 822–837.

Vanselow A. P. (1932a) Equilibria of the base-exchange reaction of bentonites, permutites, Soil colloids and zeolites. *Soil Sci.* **33,** 95–113.

Vantelon D., Pelletier M., Michot L. J., Barres O. and Thomas F. (2001) Fe, Mg and Al distribution in, the octahedral sheet of montmorillonites. An infrared study in the OH-bending region. *Clay Miner.* **36,** 369–379.

Walker G. F. (1956) The mechanism of dehydration of Mg-vermiculite. *Clays Clay Miner.* **4,** 101–115.